Proceedings of the
Annual Stability Conference
Structural Stability Research Council
Nashville, Tennessee, March 24-27, 2015

GBT-Based Assessment of the Buckling Behavior of Steel Frames Formed by Circular Hollow Section Members

Cilmar Basaglia[1], Dinar Camotim[2], Nuno Silvestre[3]

Abstract

This paper reports the results of an ongoing investigation on the use of Generalized Beam Theory (GBT) to assess the buckling behavior of thin-walled frames built from cold-formed steel circular hollow section (CHS) members. After providing an overview of the main concepts and procedures involved in performing a GBT buckling analysis, the formulation and numerical implementation of a GBT-based beam finite element are presented. Next, one addresses the constraint conditions adopted to simulate the local displacement compatibility at frame joints connecting two orthogonal CHS members. Finally, in order to illustrate the application and capabilities of the proposed GBT finite element formulation, numerical results are presented and discussed – they concern the buckling behavior of an "L-shaped" frame acted by loadings causing only member compression. For validation purposes, most GBT-based results are compared with values yielded by shell finite element analyses carried out in the code ANSYS.

1. Introduction

The extensive use of cold-formed steel circular hollow section (CHS) frames in the construction and offshore industries stems mostly from their structural efficiency (high strength-to-weight ratio), remarkable fabrication versatility and very low production and erection costs. However, since these frames often comprise very slender members, which are highly susceptible to local and global (flexural) buckling phenomena, the (numerical) assessment of their structural response constitutes a complex task (*e.g.*, Puthli *et al.* 2001, Wardenier *et al.* 2008). Indeed, rigorous numerical analyses can only be performed by resorting to shell finite element models, a time-consuming complex approach (including data input and result interpretation) still prohibitive for routine applications (*e.g.*, Zhu *et al.* 2014).

In order to make the analysis of cold-formed CHS frames computationally simpler and potentially more accessible to the average designer, without sacrificing too much the accuracy of the results obtained, it is essential to develop easy-to-use numerical tools based on beam finite element analysis. However, before this goal can be achieved, two major difficulties must be overcome: (i) include local buckling effects in a beam (1D) finite element formulation and (ii) handle the transmission of the cross-section rotation and wall transverse bending at the frame joints. A very promising alternative approach is

[1] School of Civil Eng, Architec. and Urban Design, University of Campinas, Brazil. <cbasaglia@fec.unicamp.br>
[2] ICIST, CEris, DECivil, Instituto Superior Técnico, University of Lisbon, Portugal. <dcamotim@civil.ist.utl.pt>
[3] IDMEC, DEM, Instituto Superior Técnico, University of Lisbon, Portugal <nsilvestre@tecnico.ulisboa.pt>

the use of Generalized Beam Theory (GBT), a thin-walled prismatic bar theory, originally developed by Schardt (1989), that incorporates genuine plate theory concepts, *i.e.*, accounts for the member cross-section in- and out-of-plane deformations. Moreover, the unique GBT modal nature leads to very elegant and illuminating solutions for a wealth of structural problems.

The authors have developed and numerically implemented several GBT-based beam finite elements to analyze the elastic local, distortional and global buckling behavior of plane and space frames with *open cross-sections* and *rectangular hollow section* members (*e.g.*, Basaglia *et al.* 2008, 2009, Camotim *et al.* 2010 or Camotim & Basaglia 2013).

The objective of this work is to report an ongoing investigation aimed at extending the scope of the above GBT-based approach, making is possible to analyze also the buckling behavior of steel frames formed by CHS members. A GBT-based finite element model, developed on the basis of the formulation derived by Silvestre (2007), is numerically implemented, validated and employed to perform the frame buckling analyses. Particular attention is devoted to issues concerning the determination of the finite element and overall stiffness matrices, which incorporate the effect of the frame joints. One also addresses in detail the constraint conditions modelling the displacement compatibility along the end section walls of the CHS members connected at a frame joint. In order to illustrate the application and provide a better grasp of concepts and procedures involved in the proposed GBT-based approach, numerical results are presented and discussed − they concern the buckling behavior of a cold-formed CHS "L-shaped" frame acted by loadings that cause only member axial compression. For validation purposes, most GBT-based results are compared with values yielded by rigorous shell finite element buckling analyses carried out in the commercial code ANSYS (SAS 2009).

2. GBT Buckling Analysis

In a GBT formulation, the displacement field at a given member cross-section is expressed as a linear combination of deformation modes, which makes is possible to write the equilibrium equations and boundary conditions in an unique and very convenient way − indeed, one is then able to perform a very easy and "natural" modal analysis of the cross-section deformed configuration that contributes decisively to a deeper understanding about the structural behavior under consideration. The performance of a structural analysis involves two main tasks, namely (i) a *cross-section analysis*, to identify the deformation modes and evaluate the associated modal mechanical properties, and (ii) a *member* (*or structural system*) *buckling analysis*, which consists of solving the eigenvalue problem defined by the (modal) adjacent equilibrium equation system to obtain the sought buckling response, *i.e.*, the member (or structural system) buckling load parameters and corresponding buckling mode shapes – often, only the lowest (critical) load parameters and associated buckling mode shape are required.

2.1 Formulation for CHS Members

Figure 1 depicts a prismatic member with a circular hollow section, having radius r and wall thickness t, and the global coordinate system X, Y, Z. In order to account for the cross-section in-plane deformation effects, it is preferable to consider the local coordinate system x, θ, z, (a longitudinal coordinate $x \in [0;L]$, an angular coordinate $\theta \in [0;2\pi]$ and a thickness coordinate $z \in [-t/2; +t/2]$ – u,v,w are the displacement components expressed in the local coordinate systems. In order to obtain a displacement field representation that is compatible with the classical beam theories, one must express its components $u(x,s)$, $v(x,s)$ and $w(x,s)$ as

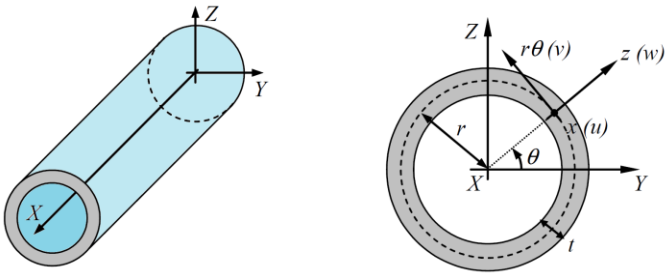

Figure 1: Circular hollow section member and global and local coordinate system and displacement components.

$$u(x,\theta) = u_k(\theta)\phi_{k,x}(x) \qquad v(x,\theta) = v_k(\theta)\phi_k(x) \qquad w(x,\theta) = w_k(\theta)\phi_k(x) \quad , \quad (1)$$

where (i) $(.)_{,x} \equiv d(.)/dx$, (ii) the summation convention applies to subscript k, (iii) $u_k(\theta)$, $v_k(\theta)$ and $w_k(\theta)$ are the functions characterizing deformation mode k (Silvestre 2007). Since the thin-walled member is deemed made of an isotropic elastic material (*e.g.*, constructional steel), the constitutive relation reads

$$\begin{Bmatrix} \sigma_{xx} \\ \sigma_{\theta\theta} \\ \tau_{x\theta} \end{Bmatrix} = \begin{bmatrix} \frac{E}{1-\nu^2} & \frac{E\nu}{1-\nu^2} & 0 \\ \frac{E\nu}{1-\nu^2} & \frac{E}{1-\nu^2} & 0 \\ 0 & 0 & G \end{bmatrix} \begin{Bmatrix} \varepsilon_{xx} \\ \varepsilon_{\theta\theta} \\ \gamma_{x\theta} \end{Bmatrix} \quad , \quad (2)$$

where (i) E, G and ν are Young's modulus, shear modulus and Poisson's ratio and (ii) σ_{ij}, ε_{ij}, γ_{ij} are the stress and strain components. As for the linear and non-linear (^{NL}) kinematical (strain-displacement) relations employed, they satisfy the Love-Kirchhoff assumption and can be expressed in terms of the mid-plane displacement components (u, v, w) as

$$\varepsilon_{xx} = u_k\phi_{k,xx} - zw_k\phi_{k,xx} \qquad \varepsilon_{\theta\theta} = \frac{v_{k,\theta} + w_k}{r}\phi_k - z\frac{w_{k,\theta\theta} - v_{k,\theta}}{r^2}\phi_k$$
$$\gamma_{x\theta} = \left(\frac{u_{k,\theta}}{r} + v_k\right)\phi_{k,x} - z\left(\frac{4rw_{k,\theta} - 3rv_k + u_{k,\theta}}{2r^2}\right)\phi_{k,x} \quad (3)$$

$$\varepsilon_{xx}^{NL} = \frac{1}{2}w_k w_i \phi_{k,x}\phi_{i,x} + \frac{1}{8}\left(v_k - \frac{u_{k,\theta}}{r}\right)\left(v_i - \frac{u_{i,\theta}}{r}\right)\phi_{k,x}\phi_{i,x} \quad . \quad (4)$$

Since the system of GBT differential equilibrium equations is established by means of the Principle of Virtual Work, expressed by

$$\delta V = \delta U + \delta \Pi \quad , \quad (5)$$

it is indispensable to consider (i) the member strain energy variation δU and (ii) the potential of the applied (pre-buckling) stresses $\delta \Pi$, which are given by

$$\delta U = \int_L \oint_t \int (\sigma_{xx}\delta\varepsilon_{xx} + \sigma_{\theta\theta}\delta\varepsilon_{\theta\theta} + \tau_{x\theta}\delta\gamma_{x\theta})dzrd\theta dx \qquad \delta \Pi = \int_L \oint_t \int (\sigma_{xx}^0 \delta\varepsilon_{xx}^{NL})dzrd\theta dx \quad , \quad (6)$$

where (i) L, r, t are the member length, cross-section mid-surface radius and thickness, respectively, and (ii) σ_{xx}^0 are pre-buckling longitudinal normal stresses caused by the axial forces and/or bending moments applied at member end sections.

It is assumed here that $\delta\Pi$ corresponds to applied loads that (i) depend linearly on a load parameter λ and (ii) cause only longitudinally uniform normal stress distributions, which are expresses as

$$\sigma_{xx}^{0} = \lambda E u_j \phi_{j,xx}^{0} \quad , \quad (7)$$

where $u_j \phi_{j,xx}^{0}$ ($j=1...4$) are the pre-buckling axial displacements fields associated with axial extension, bending and warping torsion. After introducing (2)-(4) and (7) into (6) and integrating over the cross-section (coordinates θ and z), one is led to the expressions of the five δV terms, namely

$$\delta V = \int_L (C_{ik}\phi_{k,xx}\delta\phi_{i,xx} + D_{ik}^{1}\phi_{k,x}\delta\phi_{i,x} + D_{ik}^{2}\phi_{k}\delta\phi_{i,xx} + D_{ki}^{2}\phi_{k,xx}\delta\phi_{i} + \\ + B_{ik}\phi_{k}\delta\phi_{i} + \lambda W_j^{0} X_{jik}\phi_{k,x}\delta\phi_{i,x})dx \qquad W_j^{0} = C_{jj}\phi_{j,xx}^{0} \quad , \quad (8)$$

where (i) W_j^{0} are stress resultant profiles (deemed uniform in this work) and (ii) the various matrix (or tensor) components C_{ik}, D_{ik}^{1}, D_{ik}^{2}, B_{ik} and X_{jik} are given by the expressions

$$C_{ik} = \frac{Et}{1-\nu^2}\oint (u_k u_i) r d\theta + \frac{Et^3}{12(1-\nu^2)}\oint (w_k w_i) r d\theta \quad (9)$$

$$D_{ik}^{1} = Gt\oint \left(\frac{u_{k,\theta}}{r} + v_k\right)\left(\frac{u_{i,\theta}}{r} + v_i\right) r d\theta + \frac{Gt^3}{12}\oint \left(\frac{4rw_{k,\theta} - 3rv_k + u_{k,\theta}}{2r^2}\right)\left(\frac{4rw_{i,\theta} - 3rv_i + u_{i,\theta}}{2r^2}\right) r d\theta \quad (10)$$

$$D_{ik}^{2} = \frac{\nu Et}{(1-\nu^2)}\oint \left(\frac{v_{k,\theta} + w_k}{r}\right) u_i r d\theta + \frac{\nu Et^3}{12(1-\nu^2)}\oint \left(\frac{w_{k,\theta\theta} - v_{k,\theta}}{r^2}\right) w_i r d\theta \quad (11)$$

$$B_{ik} = \frac{Et}{1-\nu^2}\oint \left(\frac{v_{k,\theta} + w_k}{r}\right)\left(\frac{v_{i,\theta} + w_i}{r}\right) r d\theta + \frac{Et^3}{12(1-\nu^2)}\oint \left(\frac{w_{k,\theta\theta} - v_{k,\theta}}{r^2}\right)\left(\frac{w_{i,\theta\theta} - v_{k,\theta}}{r^2}\right) r d\theta \quad (12)$$

$$X_{jik} = \frac{Et}{C_{jj}}\oint u_j \left(w_k w_i + \frac{1}{4}\left(v_k - \frac{u_{k,\theta}}{r}\right)\left(v_i - \frac{u_{i,\theta}}{r}\right)\right) r d\theta \quad . \quad (13)$$

It should be noted that C_{ik} are stiffness components concerning *generalised* warping and their two terms stand for the cross section primary ($u_k(\theta)$) and secondary ($w_k(\theta)$) warping effects. Note also that D_{ik} are stiffness components dealing with *generalised* twisting. Moreover, observe also that (i) matrix $[B_{ik}]$ is related to the cross-section in-plane deformation (transverse bending of the wall) and (ii) X_{jik} are the geometric stiffness components associated with the applied stress resultant W_j^{0}.

2.2 Cross-Section Analysis

The cross-section analysis comprises a set of fairly complex sequential operations, already described in detail by Schardt (1989) and Silvestre (2007). Nevertheless, it is worth drawing the reader's attention to the following aspects, concerning the concepts and procedures involved:

(i) The deformation modes consist of a "*shell-type*" mode family, an *axisymmetric* mode and a *torsion* mode.

(ii) Like the conventional deformation modes of unbranched open cross-sections (*e.g.*, Silvestre & Camotim 2002), the "shell-type" modes, based on the assumption of null membrane shear strains ($\gamma_{x\theta}$) and transverse extensions ($\varepsilon_{\theta\theta}$), constitute the core of GBT-based analysis of CHS members. Their determination is based on the expressions

$$\gamma_{x\theta}=0 \quad \Leftrightarrow \quad \frac{u_{k,\theta}}{r}+v_k=0 \qquad\qquad \varepsilon_{\theta\theta}=0 \quad \Leftrightarrow \quad \frac{v_{k,\theta}+w_k}{r}=0 \qquad , \quad (14)$$

which make it is possible to obtain the v_k and w_k displacement profiles on the sole basis of the warping (longitudinal) displacement profile u_k, *i.e.*,

$$v_k=-\frac{u_{k,\theta}}{r} \qquad\qquad w_k=-v_{k,\theta}=\frac{u_{k,\theta\theta}}{r} \qquad . \quad (15)$$

Then, by introducing (15) into (9)-(13) it becomes possible to express the tensors (stiffness matrices) exclusively in terms of u_k. In order to uncouple the member equilibrium equation system as much as possible and, at the same time, obtain stiffness matrix components with clear structural meanings, it is necessary to perform the simultaneous diagonalization of the linear stiffness matrices C_{ik} and B_{ik}, by means of a procedure described in detail by Schardt (1989). Such procedure leads to the determination of the various *shell-type* modes – the displacement profiles of mode k are defined by (the expressions are different for even and odd k values)

$$m, \quad k=2m, \quad u_{2m}=r\sin(m\theta), \quad v_{2m}=-m\cos(m\theta), \quad w_{2m}=-m^2\sin(m\theta)$$

$$m, \quad k=2m+1, \quad u_{2m+1}=r\cos(m\theta), \quad v_{2m+1}=-m\sin(m\theta), \quad w_{2m+1}=-m^2\cos(m\theta) \qquad , \quad (16)$$

where m is the number of circumferential waves exhibited by the trigonometric functions. Note that (ii$_1$) for a given m there are two similar modes with distinct order k, (ii$_2$) $m=0$ corresponds to the axial extension mode $k=1$ ($u_1=1$, $v_1=0$ and $w_1=0$) and (ii$_3$) any given $m>0$ corresponds to two similar deformation modes having distinct (consecutive) orders k. Figure 2 shows the (in-plane) deformed configurations of the first *13* shell-type modes.

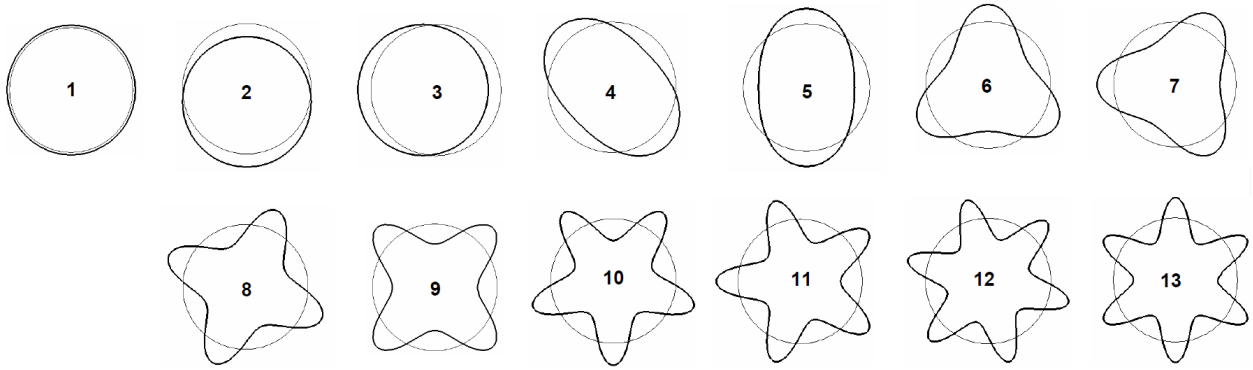

Figure 2: Shell-type deformation modes for circular hollow cross-sections.

(iii) The *axisymmetric* mode (identified by subscript **a**) involves only in-plane displacements and accounts for the cross-section deformation due to the extension in the circumferential direction – thus, the corresponding displacement profile is characterized by $u_a=0$, $v_a=0$ and $w_a=1$ (see Fig.3(a)) and is associated to the mechanical properties

$$C_{aa}=\frac{Et^3}{12(1-\nu^2)}\oint r\,d\theta \qquad D^1_{aa}=0 \qquad D^2_{aa}=0 \qquad B_{aa}=\frac{Et^3}{12(1-\nu^2)}\oint\left(\frac{1}{r^2}\right)r\,d\theta \qquad (17)$$

$$X_{jaa} = \frac{Et}{C_{jj}} \oint u_j r d\theta \quad . \quad (18)$$

(iv) The *torsion* mode (identified by subscript **t**) has a displacement profile characterized by $u_a=0$, $v_a=r$ and $w_a=0$ (see Fig.3(b)) and is associated to the mechanical properties

$$C_{tt} = 0 \qquad D_{tt}^1 = Gt \oint \left(r^2\right) r d\theta + \frac{Gt^3}{12} \oint \left(\frac{9}{4}\right) r d\theta \qquad D_{tt}^2 = 0 \qquad B_{tt} = 0 \quad (19)$$

$$X_{jtt} = \frac{Et}{C_{jj}} \oint u_j \left(\frac{1}{4} r^2\right) r d\theta \quad . \quad (20)$$

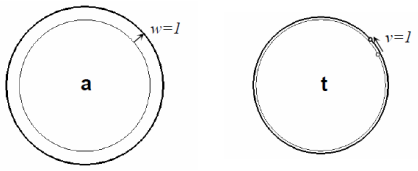

(a) (b)

Figure 3: (a) Axisymmetric (**a**) and (b) torsion (**t**) deformation modes.

(v) It is worth not that, unlike in the flat-walled cross-sections (*e.g.*, Bebiano *et al.* 2015) the GBT cross-section analysis of CHS does not need to be related to a "physical (nodal) discretization" of the cross-section (*i.e.*, no node grid has to be defined before performing the cross-section analysis). Instead, the cross-section discretization is associated with the number of circumferential waves considered to define the shell-type deformation modes (*i.e.*, the *m* value).

2.3 Member Analysis

After performing the cross-section analysis, it is possible to express the GBT equilibrium equation system in modal form as

$$C_{ik}\phi_{k,xxxx} - D_{ik}\phi_{k,xx} + B_{ik}\phi_k - \lambda\, X_{jik}^{\sigma}\left(W_j^0 \phi_{k,x}\right)_{,x} = 0 \quad , \quad (21)$$

which, together with the appropriate end support conditions (also expressed in modal form), defines the member buckling eigenvalue problem to be solved. The methods that have already been employed to solve the GBT-based eigenvalue problem are fairly standard in structural analysis. They include (i) Galerkin's method, used by Silvestre (2007) to perform the CHS member buckling analyses, and (ii) the finite element method, based on a beam element formulation specifically developed to perform GBT analyses and employed so far to analyze members exhibiting (open and/or closed) flat-walled cross-section (Silvestre & Camotim 2003[4]). At this point, it is worth mentioning that the GBT-based buckling results presented in this work have been obtained through the application of a beam finite element specifically developed for CHS members – the main steps and procedures involved in the formulation of this finite element are briefly described next:

(i) Incorporate (6) into (5), in order to obtain the variational form of the equilibrium equation system (*i.e.*, the weak counterpart of (21)), which is given by

[4] Although this GBT-based beam finite element was developed for members with unbranched open cross-sections, its extension to members exhibiting arbitrary flat-walled cross-sections is fairly straightforward and has been carried out be several authors.

$$\delta V = \int_{L_e} (C_{ik}\phi_{k,xx}\delta\phi_{l,xx} + D^1_{ik}\phi_{k,x}\delta\phi_{l,x} + D^2_{ik}\phi_k\delta\phi_{l,xx} + D^2_{ki}\phi_{k,xx}\delta\phi_l + \\ + B_{ik}\phi_k\delta\phi_l + \lambda W^0_j X_{jik}\phi_{k,x}\delta\phi_{l,x})dx \quad , \quad (22)$$

where the integrations are now carried out over the finite element length L_e.

(ii) Approximate the modal amplitude functions $\phi_k(x)$ by means of linear combinations of standard Hermite cubic polynomials (see Fig. 4),

$$\phi_k(x) = d^e_{k.1}\Psi_1(\xi) + d^e_{k.2}\Psi_2(\xi) + d^e_{k.3}\Psi_3(\xi) + d^e_{4.1}\Psi_4(\xi) \quad , \quad (23)$$

where $d^e_{k.1} = \phi_{k,x}(0)$, $d^e_{k.2} = \phi_k(0)$, $d^e_{k.3} = \phi_{k,x}(L_e)$, $d^e_{k.4} = \phi_k(L_e)$, $\xi = x/L_e$ and

$$\Psi_1 = L_e(\xi^3 - 2\xi^2 + \xi) \qquad \Psi_2 = (2\xi^3 - 3\xi^2 + 1)$$

$$\Psi_3 = L_e(\xi^3 - \xi^2) \qquad \Psi_4 = (3\xi^2 - 2\xi^3) \quad . \quad (24)$$

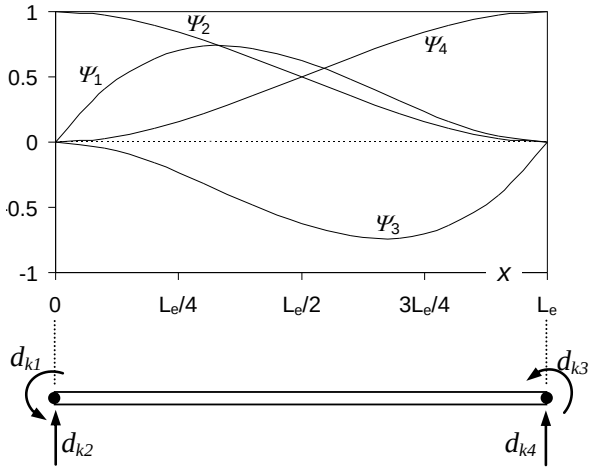

Figure 4: Finite element shape functions (Hermite cubic polynomials) and degrees of freedom adopted in the formulation of the CHS beam finite element.

(iii) The compatibility conditions must involve (iii$_1$) $d^{e.i-1}_{k.3} = \phi_{k,x}(L_e)$ and $d^{e.i}_{k.1} = \phi_{k,x}(0)$, and (iii$_2$) $d^{e.i-1}_{k.4} = \phi_k(L_e)$ and $d^{e.i}_{k.2} = \phi_k(0)$. Thus, the finite element modal generalized displacement vector is

$$d^{(e)}_k = \begin{bmatrix} d_{k1} & d_{k2} & d_{k3} & d_{k4} \end{bmatrix}^T \quad . \quad (25)$$

(iv) The corresponding finite element linear and geometric stiffness matrices are given by

$$K^{(e)}_{ik\alpha\beta} = C_{ik}\int_{L_e}\Psi_{\alpha,xx}\Psi_{\beta,xx}dx + B_{ik}\int_{L_e}\Psi_\alpha\Psi_\beta dx + D^1_{ik}\int_{L_e}\Psi_{\alpha,x}\Psi_{\beta,x}dx + \\ + D^2_{ik}\int_{L_e}\Psi_{\alpha,xx}\Psi_\beta dx + D^2_{ki}\int_{L_e}\Psi_\alpha\Psi_{\beta,xx}dx \quad (26)$$

$$G^{(e)}_{ik\alpha\beta} = W^0_j X_{jik}\int_{L_e}\Psi_{\alpha,x}\Psi_{\beta,x}dx \quad , \quad (27)$$

where the roman (i,j,k) and greek (α,β) subscripts identify the *deformation mode* and *degree of freedom* (modal generalized displacement), respectively.

(v) Taking into account the member *support conditions*, expressed in terms of the modal degrees of freedom (usually modal amplitude values and/or derivatives at the member ends – see (23)), perform the assembly procedure leading to the discrete eigenvalue problem

$$([K]-\lambda[G])\{d\}=\{0\} \quad , \quad (28)$$

where (iv1) $[K]$ and $[G]$ are the member linear and geometrical stiffness matrices, (iv2) λ is the load parameter (all applied stresses/loads depend linearly on λ) and (iv3) $\{d\}$ is the generalized modal amplitude vector – its components are the (unknown) values and/or derivatives of the GBT deformation mode amplitudes at the member nodes (finite element end cross-sections).

2.4 Illustrative Examples: Columns

In order to illustrate the concepts and procedures just presented, the GBT-based beam finite element formulation is employed to analyze the buckling behavior of CHS steel (Young's modulus *E=210GPa* and Poisson's ratio *v=0.3*) simply supported (end cross-sections locally/globally pinned and free to warp) uniformly compressed (*i.e.*, W_1^0) columns with radius *r=50mm* and wall thickness *t=1mm*. The columns are longitudinally discretised into *12* finite elements and the GBT analyses performed include *8* GBT deformation modes, namely those associated with k=**2**, **4**, **6**, **8**, **10**, **12** + **a** (axisymmetric mode) + **t** (torsion mode). For validation purposes, most GBT-based results are compared with values yielded by shell finite element analyses carried out in the code ANSYS (SAS 2009) – the columns are discretised by means of refined SHELL181 element meshes, which are employed with a "full integration" option.

First, the buckling behavior of single span columns is investigated. Figure 5 provides a schematic representation of the column discretisation and Table 1 displays (i) the critical buckling loads for columns with five lengths, obtained through GBT and ANSYS analyses, and (ii) the sole GBT deformation modes that participate in the corresponding buckling mode shape. Figure 6 shows 3-D views of the column buckling mode shapes. After observing the results given in Table 1 and Figure 6, the following conclusions may be drawn:

(i) The critical loads yielded by the GBT and ANSYS finite element analyses are virtually coincident (differences below *2.5%*). Moreover, there is also very close agreement between the buckling mode shapes provided by the two analyses (see Figs. 2, 3 and 6).

(ii) Regardless of the column length, the buckling mode shape always coincides with a single GBT deformation mode, *i.e.*, there is no coupling between the various deformation modes included in the analyses. This feature stems from the fact that all the GBT modal mechanical matrices, including X_{1ik}^{σ}, are diagonal, which means that the GBT equilibrium equations (21) are fully uncoupled.

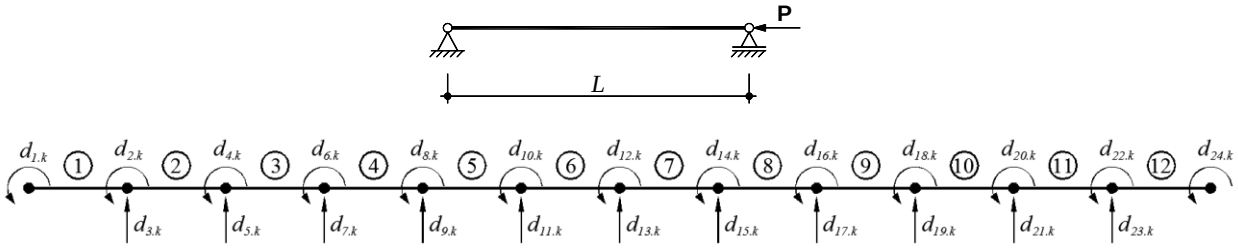

Figure 5: Column longitudinal discretization and finite element modal degrees of freedom.

Table 1: GBT and ANSYS column critical buckling loads (kN) and GBT modes participating in the buckling mode.

L (cm)	GBT	ANSYS	Δ (%)	GBT Mode
5	833.43	814.41	2.3	**a**
10	814.99	795.26	2.5	**8**
30	779.33	761.34	2.4	**6**
90	554.60	541.39	2.4	**4**
200	203.49	202.05	0.7	**2**

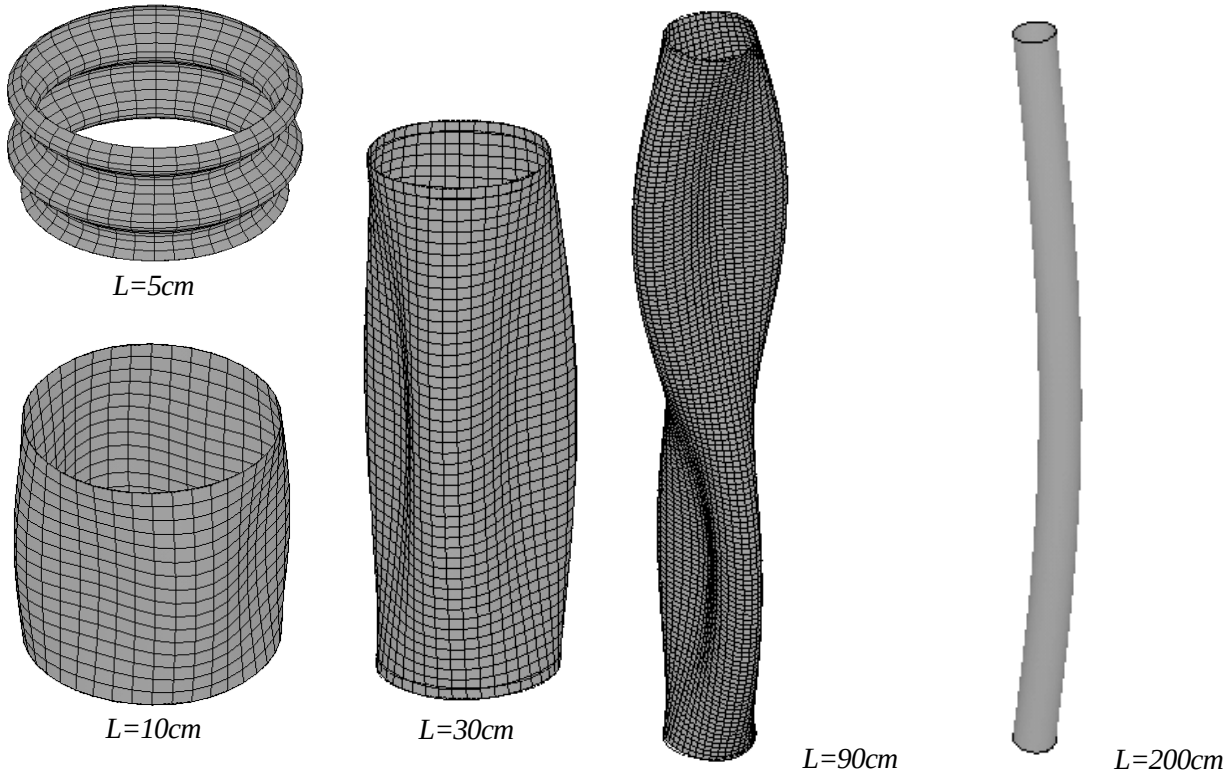

Figure 6: Critical buckling mode shapes obtained using ANSYS shell finite element analysis.

(iii) For *L=5cm*, the column buckles in a critical axisymmetric mode with *4* longitudinal half-waves.

(iv) For *L=10cm* and *L=30cm*, the column buckles in critical shell-type modes exhibiting *3* and *4* circumferential waves (*m=3* and *m=4*) and a single longitudinal half-wave. On the other hand, for *L=90cm*, buckling occurs in a critical shell-type mode with *2* circumferential waves (*m=2*) and *2* longitudinal half-waves. Finally, for *L=200cm*, the column buckles in a critical flexural mode.

The next illustrative example concerns the buckling behavior of simply supported continuous columns with three equal spans and overall lengths of *L=45,90* and *200cm*. As far as the support conditions are concerned, the columns have (i) locally and globally pinned end cross-sections that may warp freely, and (ii) cross-section with the in-plane displacements (*v* and *w*) fully restrained at the intermediate supports. Figure 7 provides a schematic representation of the three-span column discretisation and Table 2 gives their critical buckling loads and the sole GBT deformation modes participating in the critical buckling modes – Fig. 8 shows the corresponding amplitude functions $\phi_k(x)$ and the 3-D representations obtained from the ANSYS shell finite element analysis. The comparison between the GBT-based and ANSYS buckling results prompts the following remarks:

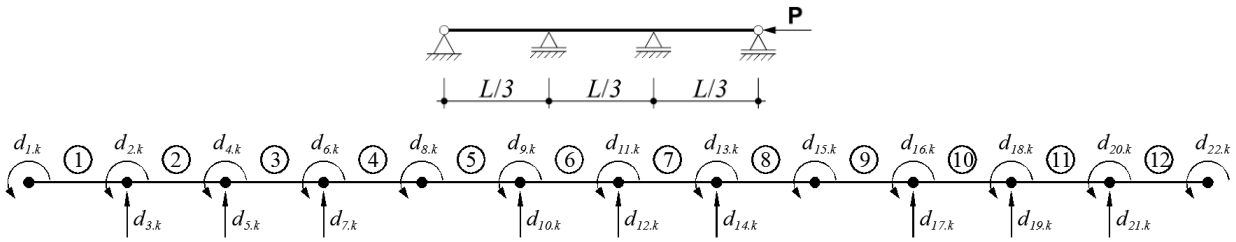

Figure 7: Three span column longitudinal discretization and finite element modal degrees of freedom.

Table 2: GBT and ANSYS buckling loads (kN) of the three span columns and GBT modes participating in the buckling mode.

L (cm)	GBT	ANSYS	Δ (%)	GBT Mode
45	809.17	791.99	2.2	**10**
90	755.70	741.34	1.9	**6**
200	515.33	506.22	1.8	**4**

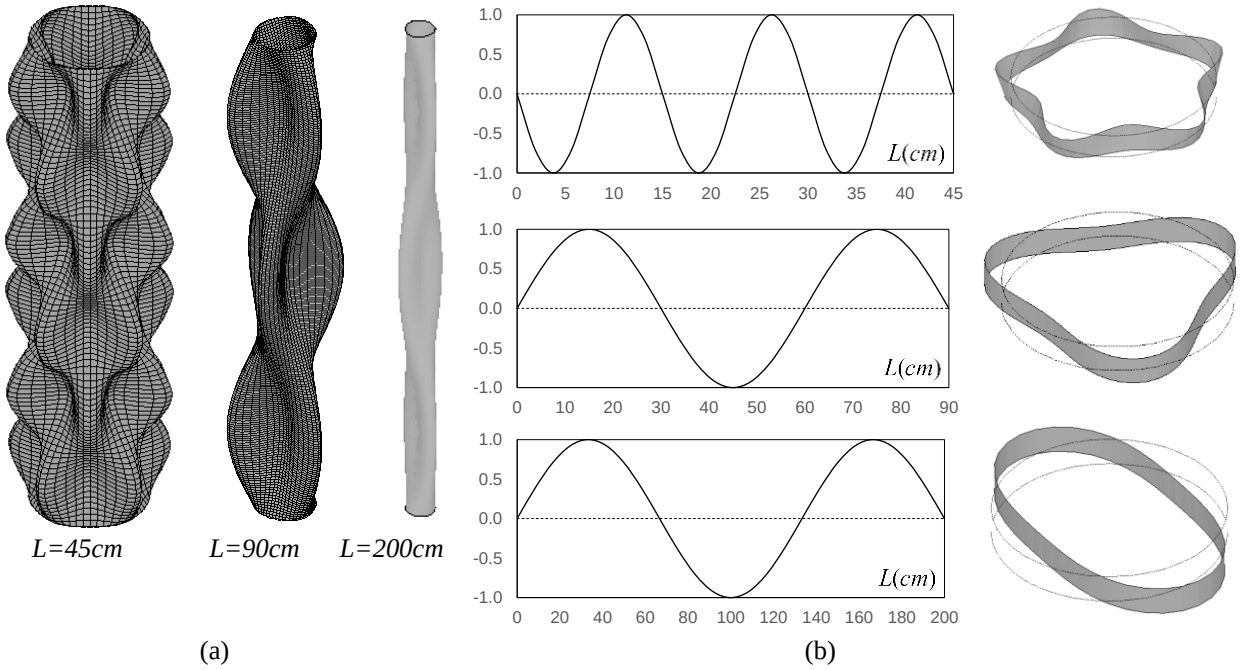

(a) (b)

Figure 8: Three-span column buckling results: (a) buckling mode shapes yielded by the ANSYS analyses and (b) modal amplitude functions $\phi_k(x)$.

(i) As in the previous case, the GBT and ANSYS critical loads are again practically coincident (once more, differences below *2.5%*).

(ii) The buckling mode shapes provided by the ANSYS analyses are in close agreement with the GBT modal amplitude functions. Like in the single span columns analyzed previously, all buckling mode shapes have contributions from a single GBT deformation mode.

(iii) In all columns, buckling occurs in shell-type modes with *2*, *3* or *5* circumferential waves (*m=2,3,5*) and *3* or *6* longitudinal half-waves.

In view of the virtual coincidence between the GBT and ANSYS buckling results concerning the two column sets analyzed, it is fair to say the GBT beam finite element formulation may be deemed validated.

3. Buckling Analysis of CHS Frames

The overall linear and geometric stiffness matrices of a given structural system are obtained by "assembling" their finite element counterparts, using the well-known "incidence matrix" concept. Although this constitutes a fairly trivial procedure for isolated members (each node shared by two equally oriented elements), its extension to frames poses several difficulties. Indeed, since the finite elements (members) connected at a frame joint exhibit different orientations (see Fig. 9(a)), it becomes necessary to account for all the effects stemming from the need to ensure compatibility between the degrees of freedom of the connected member end cross-sections (*e.g.*, nodes a_{r+1} and b_r in Fig. 9(b)). In order to overcome these difficulties, (i) it is necessary to "transform" the *modal* degrees of freedom into *nodal* ones (generalised displacements of the point where the joint is deemed materialized), by means of a "*joint element*" concept (see Fig. 9(c)), and (ii) *constraint conditions* must be imposed to enforce displacement and rotation compatibility at the connected end sections – more details can be found in the works of (i) Basaglia *et al.* (2008, 2009), for frames built from open-section members, and (ii) Basaglia & Camotim (2010), for frames built from rectangular hollow section (RHS) members.

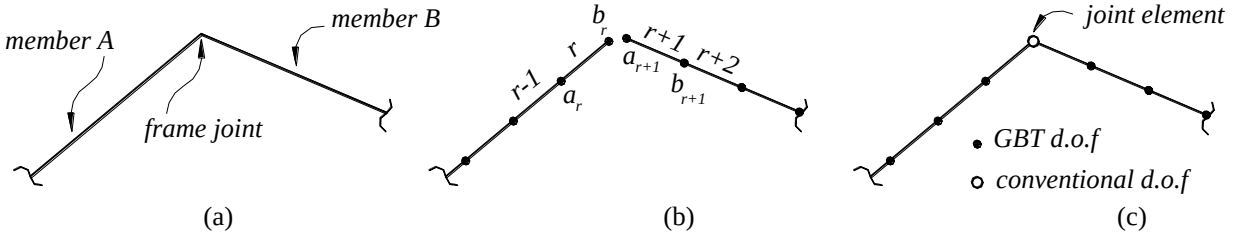

Figure 9: (a) Frame joint, (b) longitudinal discretisation of the connected members and (c) "joint element" concept.

The above constraint conditions (denoted here by Π_i) depend on the joint configuration and involve several *points* of the connected member end sections, where the joint is deemed materialized – these conditions read

$$\Pi_i = \{\Delta\}^T \{\phi_k\} = 0 \quad , \quad (29)$$

where the vector $\{\Delta\}$ components are either (i) warping functions $u_k(\theta)$ or (ii) wall flexural functions $w_k(\theta)$. The particular constraint conditions considered in this work are addressed in the next section. Once all member support and joint compatibility conditions are enforced, it is a straightforward matter to obtain the frame linear $[\widetilde{K}]$ and geometric $[\widetilde{G}]$ stiffness matrices, which are expressed in terms of "*mixed*" degrees of freedom (GBT modal and "conventional" nodal ones). The joint compatibility is incorporated into the stiffness matrix through the operation

$$\left([\widetilde{K}] + \lambda [\widetilde{G}]\right) = [\Omega]^T \left([K] + \lambda [G]\right) [\Omega] \quad , \quad (30)$$

where (i) λ is the frame *load parameter*, (ii) the tilde (~) identifies the stiffness matrices with joint compatibility conditions and (iii) the compatibility matrix $[\Omega]$, defined by

$$\{d\} = [\Omega] \{\widetilde{d}\} \quad , \quad (31)$$

contains the joint modal displacement values – $\{\widetilde{d}\}$ is a "mixed" vector combining nodal generalised displacements and modal GBT degrees of freedom.

After determining the frame total stiffness matrix ($[\widetilde{K}]+\lambda[\widetilde{G}]$), it is necessary (i) to solve the buckling eigenvalue problem and (ii) to transform the nodal degrees of freedom (joint generalised displacements) back into GBT ones, through the operation defined in (31) – this last procedure makes it possible to obtain a *fully modal* representation of the frame buckling modes (*i.e.*, identify and quantify the individual contributions of the various member deformation modes), a feature providing a decisive contribution towards a more in-depth understanding of the mechanical aspects involved in the local and global buckling behavior of thin-walled frames.

At this stage, it is worth noting that the well-known *Lagrange multiplier* technique (*e.g.*, Zienkiewicz & Taylor 2000) provides an elegant and rather efficient alternative to include the aforementioned constraint conditions into the frame buckling analysis (Basaglia 2010) – one is then led to the eigenvalue problem

$$\begin{bmatrix} [K+\lambda G] & \{\Delta\}_1 & \cdots & \{\Delta\}_i \\ \{\Delta\}_1^T & & & \\ \vdots & & 0 & \\ \{\Delta\}_i^T & & & \end{bmatrix} \begin{Bmatrix} \{d\} \\ \gamma_1 \\ \vdots \\ \gamma_i \end{Bmatrix} = \begin{Bmatrix} 0 \\ \Pi_1 \\ \vdots \\ \Pi_i \end{Bmatrix} \quad , \quad (32)$$

where γ_i is the Lagrange multiplier associated with the constraint condition *i*.

3.1 Constraint Conditions for a Joint Connecting Two Orthogonal CHS Members

Consider the unstiffened joint schematically depicted in Figure 10(a), connecting two identical orthogonal CHS members. Whenever these members experience wall bending, the shell finite element model shown in Figure 10(b) provides evidence concerning the displacement compatibility conditions that must be satisfied at the intersections of the circumferences C1–C6, C2–C5 and C3–C4 of the connected member end cross-sections – these conditions, as well as the constraint equations adopted to simulate them (approximately), are individually addressed next:

(i) *Circumferences C1 and C6*. These conditions concern the intersection of the circumferences C1 and C6 (point III in Figs. 10(a) and 10(c)), *i.e.*, the equality between the transverse bending displacements $w(x_{III},\theta_{III})$ of one member and the warping displacements $u(x_{III},\theta_{III})$ of the other. Therefore, two constraint conditions (Π^1_{III}) involving points III_A (point III in member A) and III_B (point III in member B) must be imposed – they read

$$\Pi^1_{III_A} = \sum_k u_k(\theta_{III_A})\phi_{k,x}(x_{III_A}) - \sum_k w_k(\theta_{III_B})\phi_k(x_{III_B}) = 0 \quad (33)$$

$$\Pi^1_{III_B} = \sum_k u_k(\theta_{III_B})\phi_{k,x}(x_{III_B}) - \sum_k w_k(\theta_{III_A})\phi_k(x_{III_A}) = 0 \quad . \quad (34)$$

(ii) *Circumferences C2 and C5, C3 and C4*. These conditions concern the equality between the transverse bending displacements (ii_1) at the intersection between circumferences C2 and C5 (points II and II' in Fig. 10(c)) and (ii_2) at the intersection between circumferences C3 and C4 (points I and I' in Fig. 10(a)). Thus, constraint equations (ii_1) Π^2_{II} involving points II_A, II'_A, II_B and II'_B (points II and II' in the members A and B) and (ii_2) Π^2_I involving points I_A, I'_A, I_B and I'_B (points I and I' in the members A and B) must be imposed – they read

$$\Pi_{II}^{2} = \sum_{k} w_k(\theta_{II_A})\phi_k(x_{II_B}) - \sum_{k} w_k(\theta_{II_B})\phi_k(x_{II_B}) = 0 \quad (35)$$

$$\Pi_{I}^{3} = \sum_{k} w_k(\theta_{I_A})\phi_k(x_{I_B}) - \sum_{k} w_k(\theta_{I_B})\phi_k(x_{I_B}) = 0 \quad . \quad (36)$$

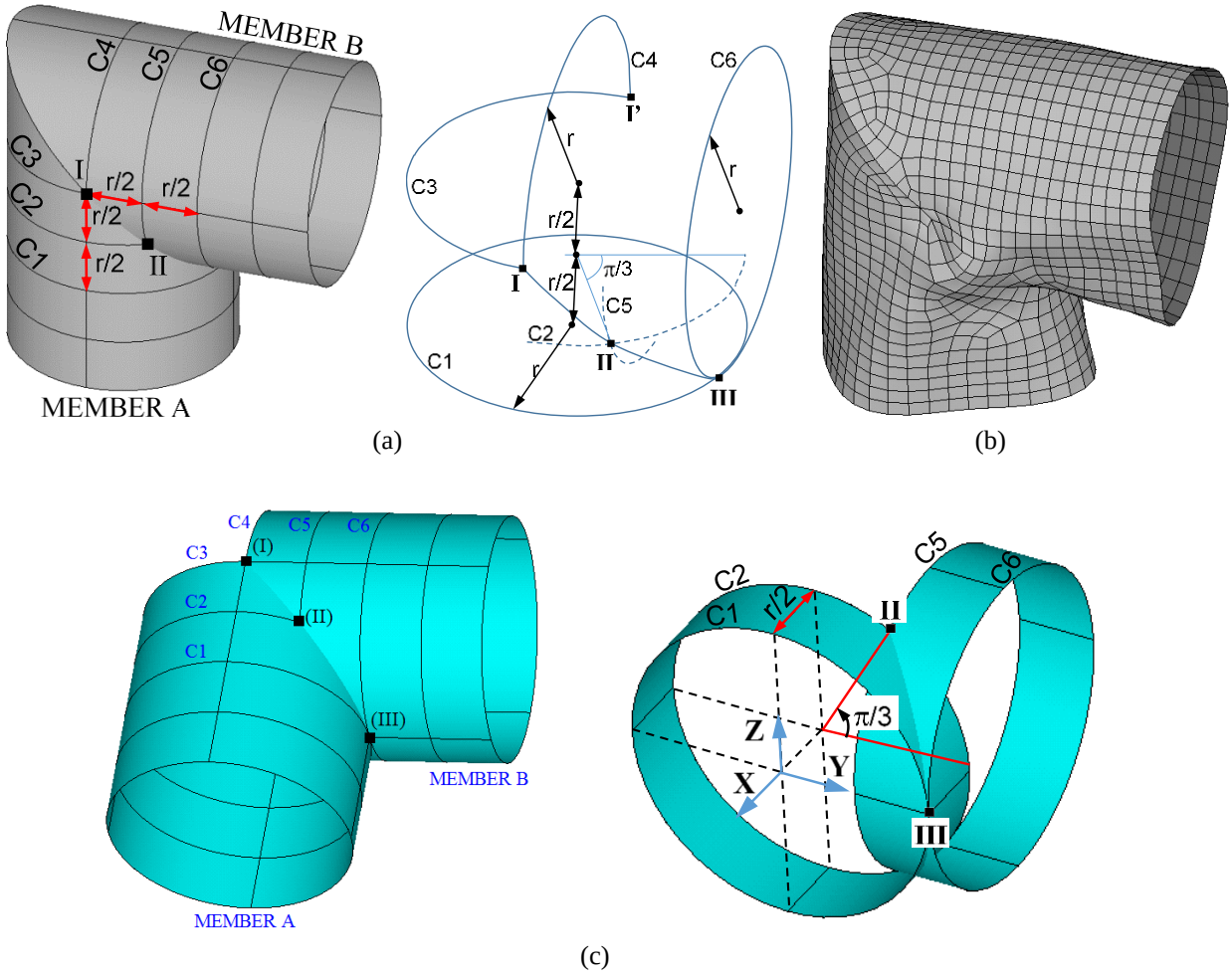

Figure 10: Unstiffened joint connecting two orthogonal CHS members (CHS knee joint): (a) overall configuration and definition of the relevant circumferences, (b) shell finite element modeling of the end cross-section displacement compatibility and (c) location of the end cross-section points where the joint is deemed materialized.

3.2 Illustrative Example: "L-shaped" Frame

In order to validate and illustrate the application and capabilities of the proposed GBT-based beam finite element approach to analyze frames, numerical results concerning the elastic buckling behavior of the "L-shaped" frame depicted in Figure 11 are presented and discussed next. The frame is formed by two orthogonal CHS steel (Young's modulus $E=210GPa$ and Poisson's ratio $\nu=0.3$) members A and B ($L_A=L_B=60cm$), with radius $r=50mm$ and wall thickness $t=1mm$, and acted by two equal axial loads P The two members are connected by an unstiffened knee joint and have locally and globally pinned end cross-sections that may also warp freely. As was done for the isolated columns, most GBT-based results (frame critical buckling loads and mode shapes) are compared with values yielded by shell finite element analyses. It is worth noting that the geometry of this frame was chosen in order to ensure a high susceptibility to local deformations (wall flexure) in both members and at the joint vicinity.

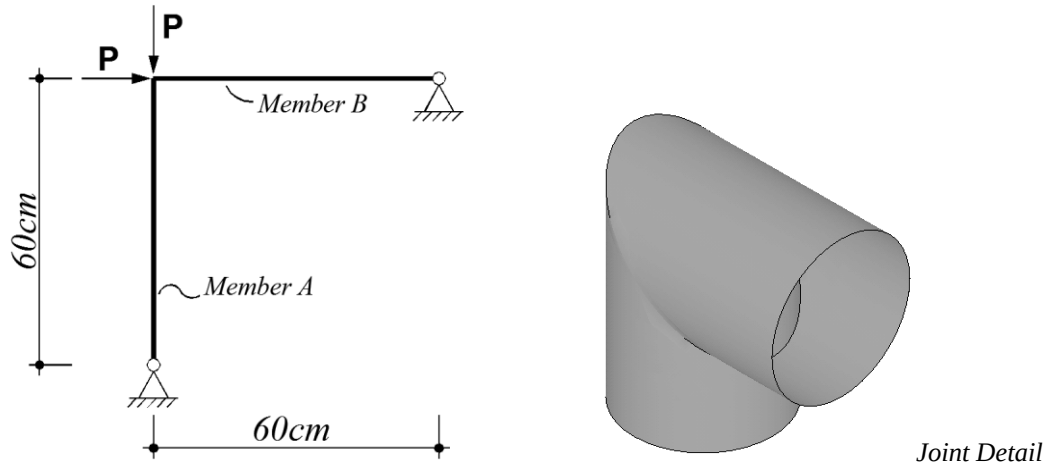

Figure 11: "L-shaped" frame formed by orthogonal CHS members: geometry, loading and support boundary, and joint detail.

While Figure 12 provides the member *A* and *B* modal amplitude functions defining the frame critical buckling mode, Figure 13 displays the corresponding configurations obtained by means of the (i) GBT-based beam finite element analysis and (ii) ANSYS shell finite element analysis – it should be stressed that the former is a 3-D representation of *beam* finite element results.

First of all, it should be pointed out that (i) the GBT and ANSYS frame critical buckling loads are virtually coincident ($P_{cr.GBT}$=*498.58kN* and $P_{cr.ANSYS}$=*482.70kN – 3.3%* difference) and it (i) the degrees of freedom numbers involved in the two analyses are orders of magnitude apart: *46500* (ANSYS) and *500* (GBT – *10* deformation modes and *12* beam finite elements in each member). Moreover, the comparison between the two buckling mode shape representations prompts the following remarks:

(i) The 3-D views of the frame buckling mode shape shown in Figure 13 are remarkably similar. In addition, there is also a very close agreement between the ANSYS buckling mode shape and the GBT modal amplitude functions displayed in Figure 12 – note, however, that the latter representation provides deeper insight on the mechanics of frame buckling.

(ii) Unlike the isolated columns previously analyzed, the frame critical buckling mode involves contributions from various deformation modes. This stems from the fact that the GBT equilibrium equations are coupled, due to incorporation of the joint displacement compatibility conditions.

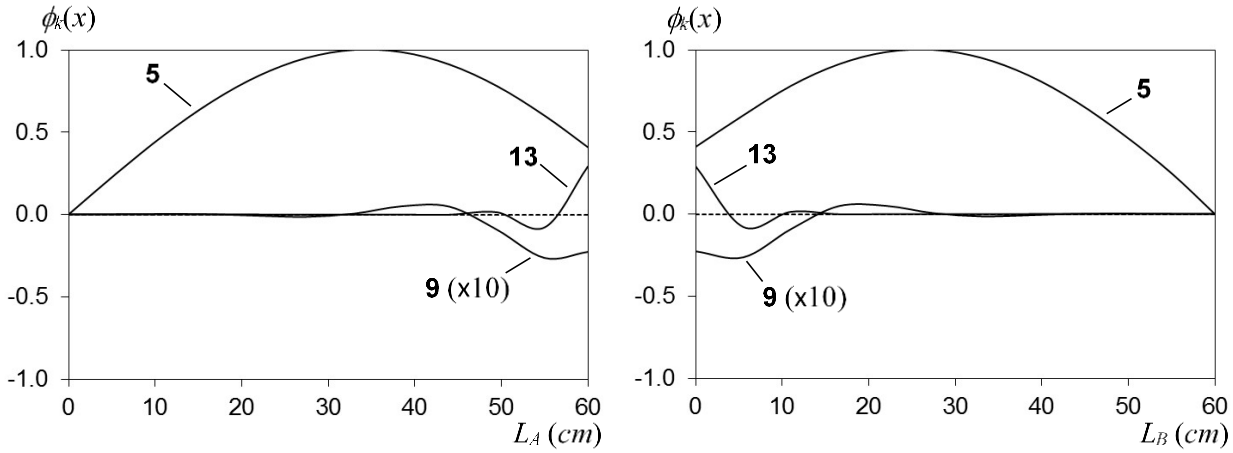

Figure 12: "L-shaped" frame GBT modal amplitude functions $\phi_k(x)$ of members A and B.

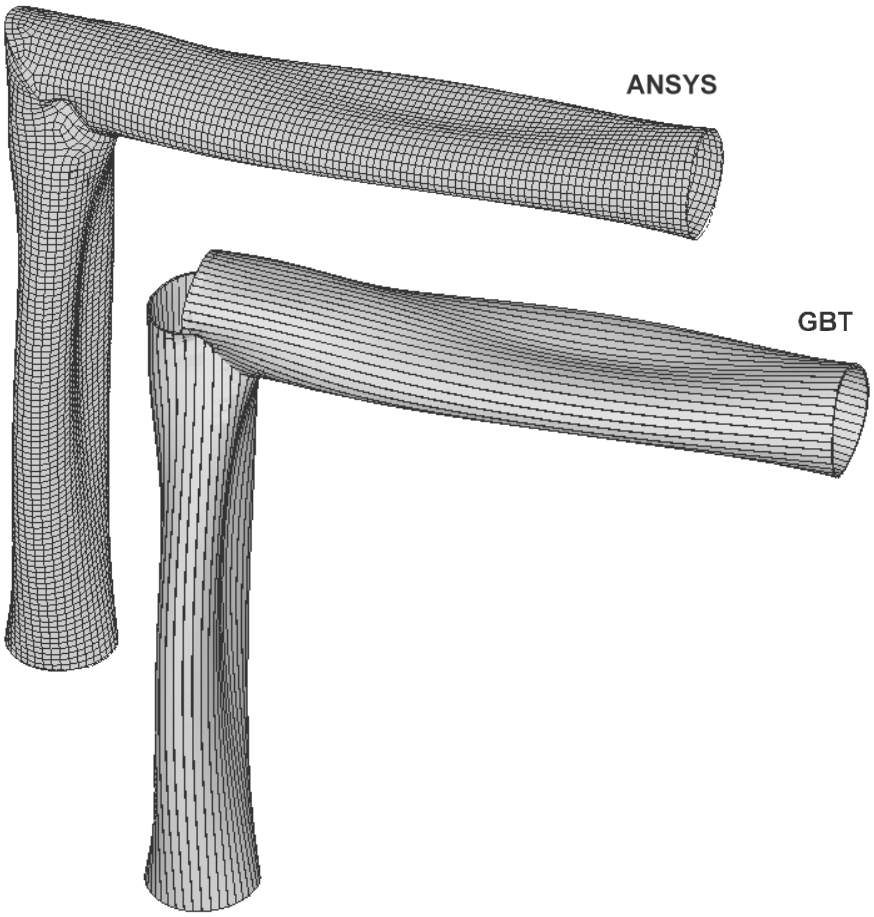

Figure 13: "L-shaped" frame buckling mode shape representations yielded by the ANSYS and GBT analyses.

(iii) The frame critical buckling occurs in a shell-type mode that (iii$_1$) involves both members equally (iii$_2$) combines participations from the GBT deformation modes **5, 9** and **13** (see Fig. 2). Mode **5** provides the clearly dominant contribution, which has maximum values in the close vicinity of each member mid-span. Moreover, there is also a non-negligible contribution from mode **13**, located in the neighborhood of the joint and exhibiting a maximum value at the joint itself. Finally, there is still a barely detectable contribution from mode **9** that has a maximum value near the joint and extends a bit further than its mode **13** counterpart – about *1/3* of the length.

(iv) The insight on the frame critical buckling mode characteristics presented in the previous item could only be acquired due the unique modal features exhibited by the GBT analyses – indeed, it would be virtually impossible to acquire such a rich insight on the frame buckling mechanics through the ANSYS shell finite element results.

4. Conclusion

The paper reported the results of an ongoing investigation on the use of a GBT-based beam finite element approach to analyze the buckling behavior of thin-walled steel frames built from CHS members. After a very brief review of the most relevant concepts involved in performing a GBT buckling analysis in CHS members, with particular emphasis on the cross-section analysis, the formulation and numerical implementation and application (to isolated columns) of a GBT-based beam finite element

were presented and discussed. Then, the paper turned its attention to frames with CHS members and described the procedures involved in obtaining the frame overall linear and geometric stiffness matrices, which must incorporate the effects stemming from the presence of the frame joints. Next, constraint conditions were established to enable modeling the displacement compatibility at the walls of the CHS unstiffened knee joint. Finally, the application and capabilities of the developed GBT-based beam finite element approach were illustrated by means of the presentation and discussion of numerical results concerning the buckling behavior of an "L-shaped" frame with axially compressed members. For validation purposes, these results were compared with values yielded by shell finite element analyses carried out in the code ANSYS. An excellent agreement was found, despite the large difference between the numbers of *d.o.f.* involved in the two analyses. It seems fair to argue that the numerical results presented, concerning both the isolated columns and the frame, provide clear evidence that GBT-based beam finite element approach to perform buckling analyses of CHS members and structural systems is as (i) numerically efficient and (ii) structurally illuminating as its predecessors, valid for members and structural systems with flat-walled cross-sections.

The authors are currently working on the establishment and validation of constraint conditions that make it possible to model the wall displacement compatibility at joints connecting either two non-orthogonal or more than two CHS members. Once this (difficult) task is completed, it will become possible to apply the developed GBT-based beam finite element approach to the buckling analysis of a much wider variety of CHS structural systems, including space (3D) frames and plane/space trusses.

References

Basaglia C (2010). *Non-Linear Analysis of Thin-Walled Steel Members and Frames Using Generalised Beam Theory*, Ph.D. Thesis in Civil Engineering, IST – Technical University of Lisbon, Portugal. (Portuguese).

Basaglia C, Camotim D. (2010). Buckling analysis of cold-formed RHS frames using Generalised Beam Theory, *Proceedings of 13th International Symposium on Tubular Structures* (ISTS-13 – Hong Kong, 15-17/12), B. Young (ed.), CRC Press (Boca Raton), 187-195.

Basaglia C, Camotim D, Silvestre N (2008). Global buckling analysis of plane and space thin-walled frames in the context of GBT, *Thin-Walled Structures*, **46**(1) 79-101.

Basaglia C, Camotim D, Silvestre N (2009). GBT-based local, distortional and global buckling analysis of thin-walled steel frames, *Thin-Walled Structures*, **47**(11) 1246-1264.

Bebiano R, Gonçalves R, Camotim D (2015). A cross-section analysis procedure to rationalise and automate the performance of GBT-based structural analyses, *Thin-Walled Structures*, in press.

Camotim D, Basaglia C (2013). Buckling analysis of thin-walled steel structures using generalized beam theory (GBT): state-of-the-art report, *Steel Construction*, **6**(2) 117-131.

Camotim D, Basaglia C, Silvestre N (2010). GBT buckling analysis of thin-walled steel frames: a state-of-the-art report, *Thin-Walled Structures*, **48**(10-11), 726-743.

Puthli R, Herion S, Karcher D (2001). *L-Joints Made of CHS and RHS Under Fatigue Loading*, Final Report, CIDECT Project 7S, University of Karlsruhe, Germany.

SAS (Swanson Analysis Systems Inc.) (2009). *ANSYS Reference Manual* (version 12).

Schardt R (1989). *Verallgemeinerte Technishe Biegetheorie*, Springer-Verlag (Berlin). (German)

Silvestre N (2007). Generalised beam theory to analyse the buckling behaviour of circular cylindrical shells and tubes, *Thin-Walled Structures*, **45**(2) 185-198.

Silvestre N, Camotim D (2002). First order Generalised Beam Theory for arbitrary orthotropic materials, *Thin-Walled Structures*, **40**(9) 755-789.

Silvestre N, Camotim D (2003). GBT buckling analysis of pultruded FRP lipped channel members, *Computers & Structures*, **81**(18-19) 1889-1904.

Wardenier J, Kurobane Y, Packer JA, van der Vegte A, Zhao X-L (2008). *Design Guide For Circular Hollow Section (CHS) Joints Under Predominantly Static Loading*, CIDECT Design Guide 1 (2nd edition), LSS Verlag.

Zhu L, Zhao Y, Shuwen L, Huang Y, Ban L (2014). Numerical analysis of the axial strength of CHS T-joints reinforced with external stiffeners, *Thin-Walled Structures*, **85**(December), 481-488.

Zienkiewicz OC, Taylor RL (2000). *The Finite Element Method* (5th edition), Butterworth-Heinemann (Oxford).